EDGE ARTICLE

Arresting dissolution of two-dimensional metal–organic frameworks enables long life in electrochemical devices†

Gopi M. R. Dontireddy,[a] Satya Prakash Suman,[a] Jose L. Merino-Gardea,[a] Tianyang Chen, [b] Jin-Hu Dou [*c] and Harish Banda [*a]

Two-dimensional conjugated metal–organic frameworks (2D cMOFs) are emerging as promising materials for electrochemical energy storage (EES). Despite considerable interest, an understanding of their electrochemical stability and the factors contributing to their degradation during cycling is largely lacking. Here we investigate three Cu-based MOFs and report that the dissolution of 2D cMOFs into electrolytes is a prevalent and significant degradation pathway. Several factors, such as the inherent solubility of ligands in electrolyte solvents and the duration of charge–discharge cycling exert a strong influence on the dissolution process. When these factors combine within a MOF, severely limited cycling stability is observed, with dissolution accounting for up to 80% of capacity degradation. Conversely, excellent cycling stability is observed when testing a Cu-MOF with a sparingly soluble ligand within an optimized potential window. Overall, these findings represent essential insights into the electrochemical stability of 2D cMOFs, offering crucial guidelines for their targeted development in EES applications.

Introduction

Two-dimensional conjugated metal–organic frameworks (2D cMOFs) are an emerging class of electrically conducting, porous crystalline materials.[1–3] Typically, 2D cMOFs host multitopic π-conjugated aromatic ligands in square planar MX_4 (X = O, NH, or S) linkages that repeat and create porous 2D sheets. Various 2D cMOFs have been synthesized using ligands with core structures ranging from benzene[4–12] to larger structures[13–17] like triphenylene,[18–22] coronene,[23] phthalocyanine,[24,25] and hexa-cata-hexabenzocoronene.[26] This structural versatility, coupled with favorable physical properties and the potential for redox activity from both ligands and metal nodes, has prompted the exploration of 2D cMOFs as electrode materials for electrochemical energy storage (EES). Several 2D cMOFs have demonstrated different EES mechanisms, including electric double-layer storage, battery-like faradaic processes, and rapid pseudocapacitance.[27–29] Organic ligands that would otherwise dissolve into the electrolytes are considered to be immobilized within 2D frameworks and participate in the EES processes.[4,30]

Notably, Cu-based MOFs have attracted significant attention due to their accessible redox activity on both ligands and Cu nodes (Cu^{2+}/Cu^+ redox couple), leading to enhanced EES.[30–37] However, investigations into the factors that determine the electrochemical stability of 2D cMOFs and lead to their capacity loss during charge–discharge cycling are rare.[3] A comprehension of the degradation pathways in 2D cMOFs is crucial for devising strategies to enhance their stability, meeting the thresholds of thousands to hundreds of thousands of charge–discharge cycles needed for EES applications in batteries and supercapacitors, respectively.

Previous studies on 2D cMOFs for EES primarily evaluated their electrochemical stability by examining the crystallinity of cycled electrodes using powder X-ray diffraction (PXRD) analyses.[27,33] Typically, the retention or loss of crystallinity in PXRD patterns of cycled electrodes is directly correlated to capacity loss. While these studies are useful in providing a rapid diagnosis of the cycled electrodes, they do not reveal underlying causes of capacity loss. Indeed, an amorphous-like PXRD pattern may result from various phenomena. For instance, processes such as the pulverization of microcrystalline electrode powders, dissolution of electrode material into electrolytes, and crystalline-to-amorphous phase transformations during charge–discharge cycling can all reduce crystallinity in the PXRD patterns. However, each of these processes can influence capacities differently. Other studies examining 2D cMOFs in two-electrode symmetric cells have provided consolidated observations of capacity losses at the cell level.[28,36] Although these studies are useful for simulating practical

aDepartment of Chemistry and Biochemistry, The University of Texas at El Paso, El Paso, Texas, 79968, USA. E-mail: hbanda1@utep.edu

bDepartment of Chemical Engineering, Stanford University, Stanford, California, 94305, USA

cSchool of Materials Science and Engineering, Peking University, Beijing, 100871, China. E-mail: doujinhu@pku.edu.cn

† Electronic supplementary information (ESI) available. See DOI: https://doi.org/10.1039/d4sc02699c

devices, they cannot provide a detailed understanding of individual electrode-level processes. Overall, understanding capacity losses and the underlying degradation pathways is essential for the targeted development of 2D cMOFs for EES.

Herein, we examine the electrochemical charge storage behavior and cycling stability of three catecholate-based Cu-MOFs, which demonstrate reversible redox activity on the [CuO$_4$] units. Through comprehensive post-mortem analyses of the electrolytes, we find that the primary cause of capacity loss during cycling is the dissolution of MOFs. Ligands with high solubility in the electrolytes result in rapid degradation of MOF performance, whereas ligands with low solubility promote stable cycling. A control of the experimental conditions and the electrochemical parameters is shown to exert a crucial influence on the dissolution, and the cycling stability of 2D cMOFs.

Results

Three Cu-based MOFs were synthesized with increasingly larger aromatic cores progressing from tetrahydroxy-1,4-benzoquinone (THQ) to 2,3,6,7,10,11-hexahydroxytriphenylene (HHTP) and 2,3,7,8,12,13-hexahydroxytetraazanaphthotetraphene (HHTT) using the reported procedures.[10,19,38,39] (Schemes 1–3) Powder X-ray diffraction patterns (PXRDs) of the synthesized powders confirmed the crystallinity and phase purity of the three Cu-MOFs (Fig. S1†). In all cases, copper ions (a mixture of Cu^{2+} and Cu$^+$) bond with two neighboring ligands, forming square planar [CuO$_4$] secondary building units that repeat to generate planar, porous sheets. These sheets are stacked in eclipsed or slip-stacked arrangements, thereby creating 1D pores (Cu$_3$HHTT$_2$ shown in Fig. 1a).[38] The electrochemical behavior of the three MOFs was investigated in Swagelok-type cells using a three-electrode cell configuration and electrodes prepared with 80% active materials (details in methods). Because the focus of this report is on revealing general degradation pathways for 2D cMOFs, electrochemical tests on all MOFs were performed in similar potential windows above 2.4 V *vs.* Li$^+$/Li or −0.7 V *vs.* Ag/AgCl. These potential ranges mainly accommodate the redox processes that occur on the [CuO$_4$] units and do not involve deep reduction of aromatic cores.[12,22,31–34,36] The redox activity of Cu$_3$THQ$_2$ and Cu$_3$HHTP$_2$ were previously studied in these cathodic potentials, however, Cu$_3$HHTT$_2$ has not been explored.

Cyclic voltammograms (CVs) of Cu$_3$HHTT$_2$ recorded at a scan rate of 2 mV s^{-1} in aqueous and acetonitrile (ACN) electrolytes (0.5 M NaClO$_4$) both displayed two sets of reversible redox peaks and matched well with a theoretical capacity of ∼80 mA h g^{-1} calculated for a three-electron reduction per Cu$_3$HHTT$_2$ (molecular weight 1010 g mol^{-1}, ESI Table 1). Moreover, CVs recorded over a range of scan rates exhibited excellent power capability, with a capacity of ∼63 mA h g^{-1} at 25 mV s^{-1} (Fig. 1c and S2†). Additionally, an evaluation of the electrode kinetics using scan rate *versus* peak current analysis (eqn (1), where *i* is the peak current, *v* is the scan rate, and *a* and *b* are adjustable parameters) found *b* values close to 0.9 in both aqueous and non-aqueous electrolytes. These *b* values, close to unity, indicate that the charge storage in Cu$_3$HHTT$_2$ can be characterized as a rapid, pseudocapacitive process.[40]

$$i(v) = av^b \tag{1}$$

The origins of the two distinct redox events observed for Cu$_3$HHTT$_2$ in NaClO$_4$/ACN were investigated by analyzing X-ray
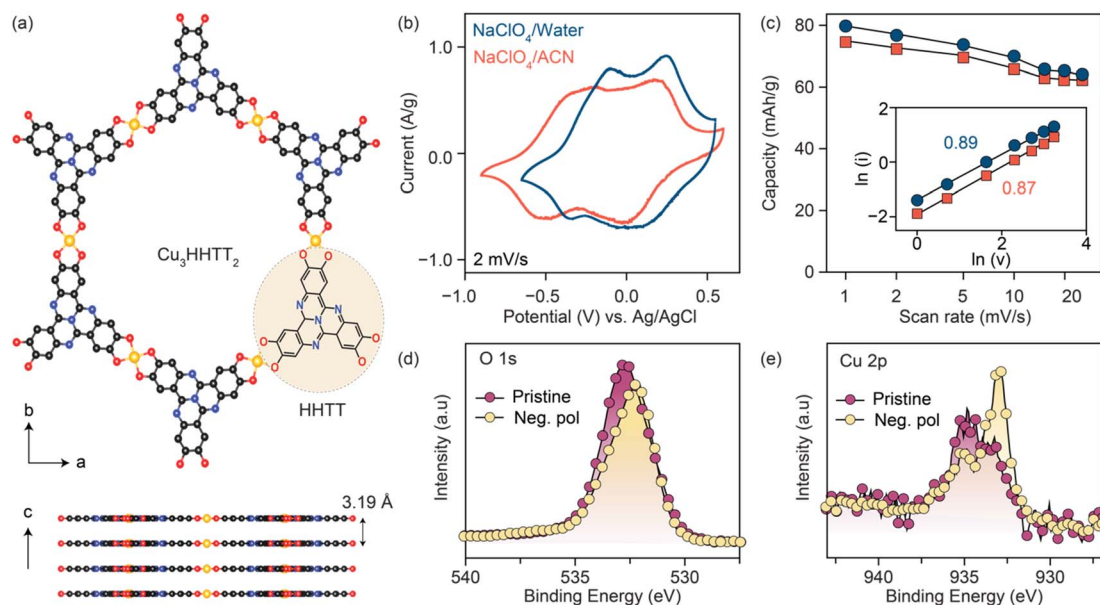
Fig. 1 (a) Crystal structure of Cu$_3$HHTT$_2$ shown in *ab* plane and along the *c* axis. (b) Cyclic voltammetry curves of Cu$_3$HHTT$_2$ were recorded at a scan rate of 2 mV s^{-1} in 0.5 M NaClO$_4$ solutions of water and acetonitrile (ACN). (c) Specific capacities were calculated from CVs recorded at scan rates ranging from 1–25 mV s^{-1} in NaClO$_4$/water and NaClO$_4$/ACN electrolytes. The inset shows power–law analysis and *b* values of 0.89 and 0.87 for Cu$_3$HHTT$_2$ in NaClO$_4$/water and NaClO$_4$/ACN, respectively. High-resolution *ex situ* X-ray photoelectron spectra of (d) O 1s and (e) Cu 2p of pristine and negatively polarized Cu$_3$HHTT$_2$ (−0.75 V *vs.* Ag/AgCl). A notable decrease in C=O and Cu^{2+} components indicates a reduction of both ligand and copper nodes under negative polarization.

photoelectron spectra (XPS) of the negatively polarized electrodes under *ex situ* conditions (Fig. 1d, e and S3†). A comparison of the high-resolution O 1s XPS data of the pristine MOF and the negatively polarized sample (-0.75 V *vs.* Ag/AgCl) reveals a decrease in intensity for the C=O component (532.3 eV) and an increase in the C–O component (531.5 eV), confirming redox activity on the ligand moieties in Cu_3HHTT_2 (Fig. 1d, deconvolution shown in S3†). Similarly, an analysis of the high-resolution Cu 2p XPS data of the pristine MOF and the negatively polarized sample at -0.75 V *vs.* Ag/AgCl (Fig. 1e, deconvolution shown in S3†) indicated an obvious enhancement in the relative composition of Cu^+ species (peaks at 932.7 and 952.2 eV for Cu $2p_{3/2}$ and Cu $2p_{1/2}$, respectively) over Cu^{2+} (peaks at 934.4 and 954.6 eV for Cu $2p_{3/2}$ and Cu $2p_{1/2}$, respectively). These results indicate that the three-electron reduction of Cu_3HHTT_2 occurs both on the HHTT moieties and the Cu nodes, consistent with previous reports on Cu-MOFs.[15,31,33]

The electrochemical stability of Cu_3HHTT_2 was investigated through galvanostatic cycling with potential limitation (GCPL) studies in both aqueous and ACN-based electrolytes. Charge–discharge profiles at a current density of 750 mA g^{-1} (or ~3 C rate, where 1 C equals full discharge in one hour) delivered discharge capacities of ~80 mA h g^{-1} with an average discharge voltage of -0.1 V *vs.* Ag/AgCl in both electrolytes (Fig. 2a). Moreover, excellent power performance was observed with discharge capacities of ~65 mA h g^{-1} at a high current density of 2 A g^{-1} or ~25 C rate (Fig. S4 and S5†). Repeated cycling of Cu_3HHTT_2 in aqueous electrolytes at current densities of 250, 500, and 750 mA g^{-1} exhibited remarkable stability over hundreds of cycles, with nearly full retention of discharge capacities (Fig. 2b). However, cycling in $NaClO_4$/ACN resulted in a significant decrease in discharge capacities, with ~70% of the initial capacity lost within 350, 500, and 950 cycles at current densities of 250, 500, and 750 mA g^{-1}, respectively. Moreover, impedance spectra recorded in between the GCPL cycles at a current density of 750 mA g^{-1} indicated little to no changes, emphasizing that the degradation in capacities observed during GCPL cycling is not caused by increasingly resistive electrodes (Fig. S6†).

It is notable that the conventional representation of cycling data, where capacity retention is plotted against the number of cycles, can potentially lead to misinterpretation, suggesting greater stability at higher cycling rates. Interestingly, an alternative representation of cycling data, plotting capacity retention against the total time of cycling, revealed strikingly similar degradation profiles for Cu_3HHTT_2 at different current densities. Specifically, results from the charge–discharge cycling of six cells in $NaClO_4$/ACN indicated a consistent capacity loss rate of 1% per hour (Fig. 2c). Overall, these results underscore the distinct cycling stability behaviors of Cu_3HHTT_2 between aqueous and ACN-based electrolytes and emphasize that the total duration of cycling governs the extent of its degradation in $NaClO_4$/ACN.

Electrode dissolution and capacity loss

Analysis of cycled Cu_3HHTT_2 electrodes using PXRD indicated that their crystallinity remained intact after 100 hours of cycling

in an aqueous electrolyte (Fig. 2d). In contrast, electrodes cycled and degraded in $NaClO_4$/ACN exhibited a notable decrease in crystallinity, resembling typical observations associated with degraded MOF electrodes. However, while these analyses are valuable in assessing the final state of cycled electrodes, they do not provide insights into the underlying causes of capacity loss. Ultraviolet-visible (UV-vis) spectroscopy was employed to examine the electrolyte solutions retrieved from cycled and disassembled cells. The UV-vis spectra of electrolytes obtained from cells cycled in $NaClO_4$/ACN showed prominent absorption peaks at 210 and 280 nm (Fig. 2e). In contrast, electrolytes from cells cycled in aqueous conditions exhibited reduced intensity around 200 nm. Notably, the pristine electrolytes themselves lack absorption features within the 200–500 nm range (Fig. S7a†), indicating that the observed absorption in cycled electrolytes stems from additional species introduced during cycling. Interestingly, a comparison of the UV-vis spectra of $CuNO_3$ and HHTT in ACN with cycled electrolytes reveals that the peaks at 210 and 280 nm corresponded to the presence of copper and HHTT, respectively. Furthermore, control experiments that recorded UV-vis spectra of sonicated solutions of Cu_3HHTT_2 in ACN did not show a similar presence of copper and HHTT (Fig. S7b†). These tests indicate that the observation of copper and HHTT in the electrolytes from cycled cells is not due to poor adhesion of MOF particles that may break off from the electrode substrate and enter the electrolyte solution. Taken together, these findings strongly suggest that Cu_3HHTT_2 disintegrates and dissolves from the electrodes into the electrolytes during cycling. Additionally, the differences in cycling stabilities and absorption spectra between $NaClO_4$/water and $NaClO_4$/ACN may then be attributed to the higher solubility of HHTT in ACN. Indeed, further GCPL studies on Cu_3HHTT_2 in electrolyte mixtures of water and ACN revealed a direct correlation, where a higher content of ACN led to rapid degradation of capacities (Fig. S8 and S9†). Overall, these results confirm that the dissolution of a MOF governs its cycling stability, and the choice of electrolyte solvent, such as ACN *versus* water, is crucial.

The validity of observations regarding the degradation and dissolution of Cu_3HHTT_2 was probed in two other Cu-based MOFs – Cu_3THQ_2 and Cu_3HHTP_2. THQ and HHTP are two commonly used organic ligands with smaller aromatic cores compared to HHTT. While HHTP and HHTT exhibit similar solubilities (~0.1 mg mL^{-1}) in water, THQ is twenty times more soluble (1.97 mg mL^{-1}) than both (Fig. 3a, details in methods). In ACN, THQ and HHTP (~0.66 mg mL^{-1}) are three times more soluble than HHTT (0.22 mg mL^{-1}). GCPL studies on Cu_3THQ_2 and Cu_3HHTP_2 revealed significant degradation within 12 hours of cycling in both aqueous and ACN-based electrolytes (Fig. 3b and S10†). Specifically, Cu_3THQ_2 degraded by 50% within the first two hours of cycling. UV-vis analysis of the retrieved electrolytes from cycled cells indicated strong absorption at wavelengths corresponding to the presence of Cu, THQ, and HHTP, respectively (Fig. S11 and S12†). Taken together, the cycling behavior and the UV-vis absorption spectra of Cu_3THQ_2 and Cu_3HHTP_2 validate that dissolution is a common pathway for the degradation of 2D cMOFs. Furthermore,
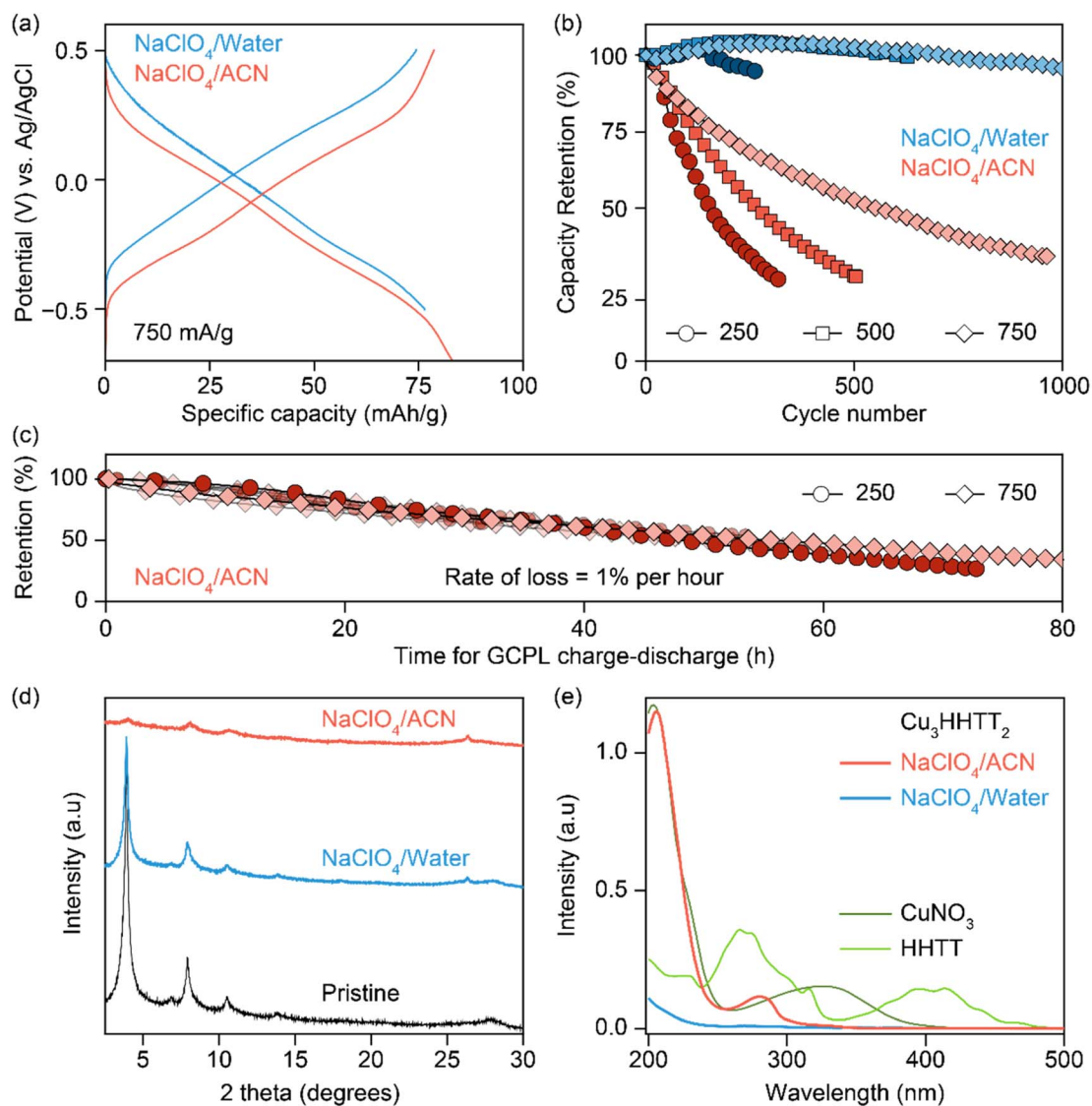
Fig. 2 (a) Charge–discharge profiles of Cu$_3$HHTT$_2$ recorded at a current density of 750 mA g^{-1} in NaClO$_4$/water and NaClO$_4$/ACN solutions. (b) Capacity retention *versus* the number of cycles for galvanostatic cycling with potential limitation (GCPL) at current densities of 250, 500, and 750 mA g^{-1} in NaClO$_4$/water and NaClO$_4$/ACN. (c) Capacity retention *versus* cumulative time of GCPL cycling in NaClO$_4$/ACN is shown for six cells, three each at 250 and 750 mA g^{-1}. All six cells display a similar degradation rate of 1% per hour. (d) Powder X-ray diffraction patterns of pristine and cycled Cu$_3$HHTT$_2$ electrodes. Electrodes cycled in NaClO$_4$/water and NaClO$_4$/ACN display a retention and loss of crystallinity, respectively. An additional peak at ~26° in the electrodes corresponds to the carbon paper substrate. (e) Ultraviolet-visible absorption spectra of electrolytes retrieved from cycled cells of Cu$_3$HHTT$_2$ in NaClO$_4$/water and NaClO$_4$/ACN, also shown are absorption spectra for solutions of HHTT and CuNO$_3$ in ACN.

a correlation emerges between ligand solubility and the performance of its corresponding MOF in an electrolyte.

Quantifying degradation

The contribution from electrode dissolution to the overall capacity loss during the cycling of 2D cMOFs was investigated by quantifying dissolved species in the electrolyte using UV-vis and inductively coupled plasma mass spectrometry (ICP-MS). Cu$_3$HHTP$_2$ was selected for analysis due to its prominence in prior studies.[33,36] UV-vis spectra of degraded Cu$_3$HHTP$_2$ cells in ACN electrolytes were compared to standard solutions prepared by mixing CuNO$_3$ and HHTP in ACN (in a 3 : 2 ratio, Fig. 4a,

details in methods, Fig. S13†). A quantitative assessment of four Cu$_3$HHTP$_2$ cells, each experiencing a loss of around 50% of their initial capacity, revealed that nearly 30% of the electrode masses were dissolved in the electrolytes. In essence, an average of 60% (ranging between 45–75%) of the capacity losses in Cu$_3$HHTP$_2$ cells could be directly linked to electrode dissolution (Fig. 4b). Additionally, ICP-MS analyses of the electrolytes from degraded Cu$_3$HHTP$_2$ cells identified a significant presence of copper, also attributing 50% (ranging between 30–80%) of the capacity losses to this dissolution process. Overall, both UV-vis and ICP-MS analyses highlight electrode dissolution as the
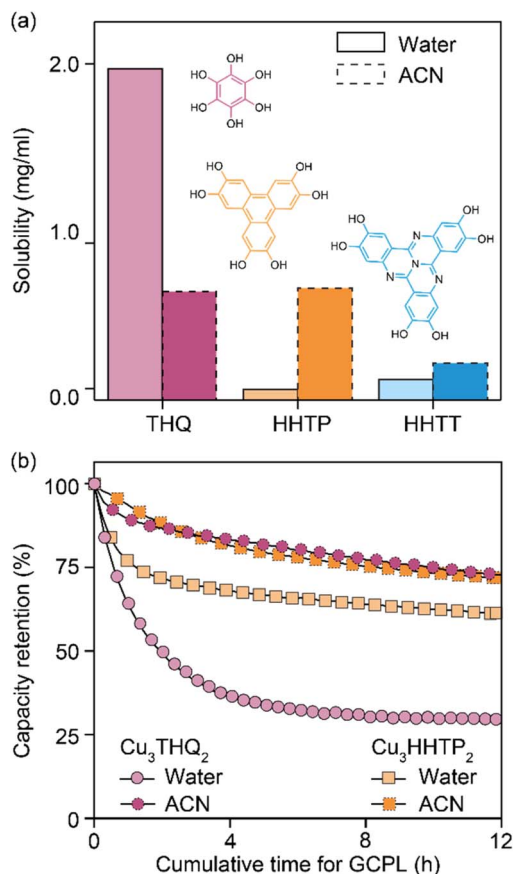
Fig. 3 (a) Solubilities of THQ, HHTP, and HHTT in acetonitrile (ACN) and water, measured at ambient conditions. (b) Capacity retention *versus* cumulative time of GCPL cycling for Cu$_3$THQ$_2$ and Cu$_3$HHTP$_2$ at a current density of 750 mA g^{-1} in NaClO$_4$/water and NaClO$_4$/ACN.
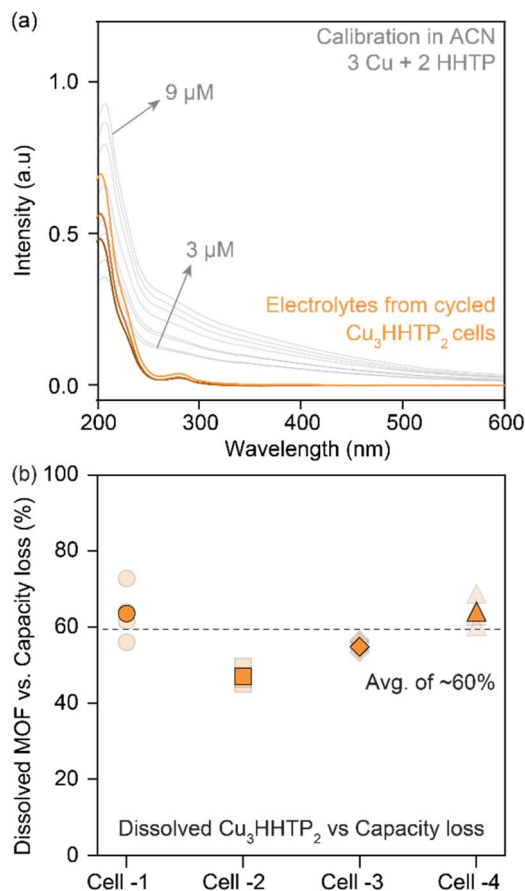

Fig. 4 (a) Ultraviolet-visible absorption spectra of electrolytes retrieved from cycled cells of Cu$_3$HHTP$_2$ in NaClO$_4$/ACN. Also shown are the absorption spectra for calibration solutions prepared by mixing CuNO$_3$ and HHTT in a ratio of 3 : 2 in ACN. (b) Quantitative estimation of the dissolved Cu$_3$HHTP$_2$ in electrolytes retrieved from four cells. An average of 60% of the total degradation can be attributed to electrode dissolution during cycling.

predominant, if not primary, mode of degradation in Cu$_3$HHTP$_2$.

Electrochemical quartz crystal microbalance (EQCM) was used to identify and examine electrode dissolution of 2D cMOFs under operando conditions (Fig. S14†). A comparison was made between the degradation of Cu$_3$THQ$_2$ and Cu$_3$HHTT$_2$ in aqueous electrolytes, representing two contrasting scenarios of cycling stability. Both MOFs were drop-casted as slurry mixtures onto gold-coated quartz crystals for EQCM tests, targeting a mass loading of 20 μg per electrode (details in methods). Initial capacities, calculated from the CVs recorded at 10 mV s^{-1} (Fig. 5a), were ~10 and ~20 mA h g^{-1} for Cu$_3$THQ$_2$ and Cu$_3$HHTT$_2$ respectively in a shorter stable electrochemical potential window of 500 mV from −0.1 to 0.4 V *vs.* Ag/AgCl. These capacities fell within the expected range from studies in Swagelok cells in corresponding potential windows, validating the relevance of the obtained results to the MOF performances. Continuous cycling of CVs revealed a rapid 68% capacity loss for Cu$_3$THQ$_2$ and comparatively stable performance for Cu$_3$HHTT$_2$. Frequency profiles obtained during the first 36 CV cycles (or cycling for 1 hour) displayed a significant increase for Cu$_3$THQ$_2$ and a relatively flat profile for Cu$_3$HHTT$_2$ (Fig. 5b). Specifically, Cu$_3$THQ$_2$ showed an average frequency increase (Δf) of ~115 Hz

across three trials, whereas Cu$_3$HHTT$_2$ exhibited an average Δf of ~5 Hz. According to the principles governing the frequency of oscillating crystals and the Sauerbery equation for EQCM (refer to ESI†), an increasing frequency (positive Δf) corresponds to a decreasing mass (negative Δm) of the crystal. These findings confirm a physical loss of electrode mass, indicating electrode dissolution during MOF cycling. Furthermore, calibration of the EQCM setup enabled the conversion of Δf ~115 Hz for Cu$_3$THQ$_2$ to a Δm of −5.5 μg, corresponding to a ~45% loss of active material. A comparison between the capacity loss from electrochemical measurements (68%) and the mass loss from EQCM measurements (45%) provided conclusive evidence supporting electrode dissolution as the primary mechanism for capacity loss in Cu$_3$THQ$_2$. Moreover, the rate of capacity loss in Cu$_3$THQ$_2$, and the corresponding increases in resonating frequency of the electrode, are highest during the first few cycles of CVs. This observation resembles the rapid capacity loss noted for Cu$_3$THQ$_2$ in the GCPL tests (Fig. 3b). A scheme representing the rapid electrode dissolution in Cu$_3$THQ$_2$ and relative stability in Cu$_3$HHTT$_2$ is shown in Fig. 5c.
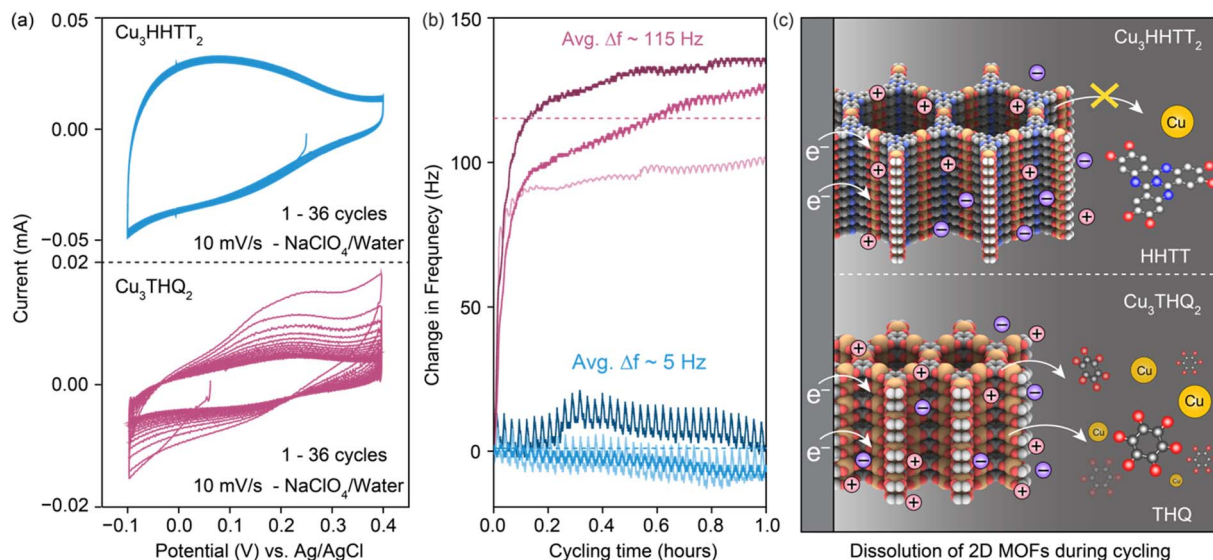
Fig. 5 (a) Cyclic voltammetry at a scan rate of 10 mV s^{-1} and (b) corresponding electrochemical quartz crystal microbalance responses from Cu$_3$HHTT$_2$ and Cu$_3$THQ$_2$ in 0.5 M NaClO$_4$/water over 36 cycles. Cu$_3$THQ$_2$ displayed a decrease in capacity (65%) and an increase in frequency (Δf ~115 Hz). The increase in frequency corresponds to a mass loss of ~5.5 µg, or ~45% of the initial deposition. On the other hand, Cu$_3$HHTT$_2$ displayed relatively stable capacities and Δf ~5 Hz. (c) Schematic depiction of the stability and dissolution of Cu$_3$HHTT$_2$ and Cu$_3$THQ$_2$ during electrochemical cycling.

Factors affecting degradation

The experimental and electrochemical parameters that govern the dissolution of Cu$_3$HHTT$_2$ were investigated to optimize its cycling stability for EES applications. First, testing Cu$_3$HHTT$_2$ cells in ACN after resting for more than 100 hours showed no degradation in its capacities, indicating sufficient insolubility of the pristine MOF in the electrolyte solution (Fig. S15†). Second, subjecting Cu$_3$HHTT$_2$ cells in ACN to a potentiostatic condition (constant voltage or CSTV) of −0.70 V *vs.* Ag/AgCl with intermittent GCPL cycling (2 cycles after every two hours under polarization) resulted in a rapid degradation behavior, faster than the GCPL condition alone (Fig. 6a and S16†). These findings indicate a significant influence of externally applied polarization and the cumulative duration of polarization during cycling on Cu$_3$HHTT$_2$ dissolution. This observation also aligns with the earlier data on the cycling behavior of Cu$_3$HHTT$_2$ under GCPL conditions, where tests at various current densities resulted in a consistent capacity loss of 1% per hour of cycling (Fig. 2c).

The influence of external polarization on the electrochemical stability of Cu$_3$HHTT$_2$ was further investigated through studies in different potential windows. GCPL cycling of Cu$_3$HHTT$_2$ in NaClO$_4$/ACN within the potential window of 0.5 to −0.1 V *vs.* Ag/AgCl (Fig. 6a, S17 and S18† labelled as half discharge), delivered remarkably stable cycling relative to the cycling performed in the full window between 0.5 to −0.7 V *vs.* Ag/AgCl (Fig. 2b). Cycling Cu$_3$HHTT$_2$ over 100 000 CV cycles or 1500 hours in this half-discharge window has also resulted in extraordinary stability (Fig. S19†). *Ex situ* XPS analyses were then performed on the half and full discharged states of Cu$_3$HHTT$_2$ to understand its stable cycling in the half-discharge window (Fig. S20†). A comparison with the pristine MOF revealed that the reduction

of Cu^{2+}/Cu$^+$ predominantly occurs in the second half of the discharge, suggesting that a high relative content of Cu^{2+} aids cycling till the half-discharged state. When this significant finding was then tested in Cu$_3$HHTP$_2$, which is known to also exhibit Cu^{2+}/Cu$^+$ reduction, cycling in both half and full discharge windows resulted in similar degradation patterns, (Fig. S21†).

These seemingly contrasting results in two MOFs, obtained in loosely defined half and full discharge potential windows, were then carefully analyzed by applying stepwise electrochemical polarization to both Cu$_3$HHTT$_2$ and Cu$_3$HHTP$_2$. Specifically, increasingly negative potentials (with 100 mV intervals) were applied for 2 h with intermediate GCPL cycling to identify the "on-set" potentials for capacity degradation in both MOFs (details in Fig. S22†). Both MOFs displayed similar capacity retention patterns *versus* applied potentials, wherein, three distinct regions can be identified. Constant potential polarizations in regions 1 and 3 resulted in minor changes to the capacities, whereas polarizations in region 2 led to a significant drop. Notably, the potentials that make up regions 1–3 are specific to each MOF. Nevertheless, the application of polarization can cause more changes to a MOF, beyond chemical reduction alone. A recent report on Cu$_3$HHTP$_2$ has revealed a reversible expansion and contraction of lattice during ion sorption in its pores.[33] The influence of the mechanical strain originating from such structural changes on cycling stability will likely vary between different MOFs.

Avoiding redox contributions from region 2 for enhanced capacity retention leads to lower storage capacities for MOFs. We sought to maintain the redox activity in Cu$_3$HHTT$_2$ while addressing its dissolution through control of the experimental parameters. Specifically, HHTT has a low solubility of 0.22 mg
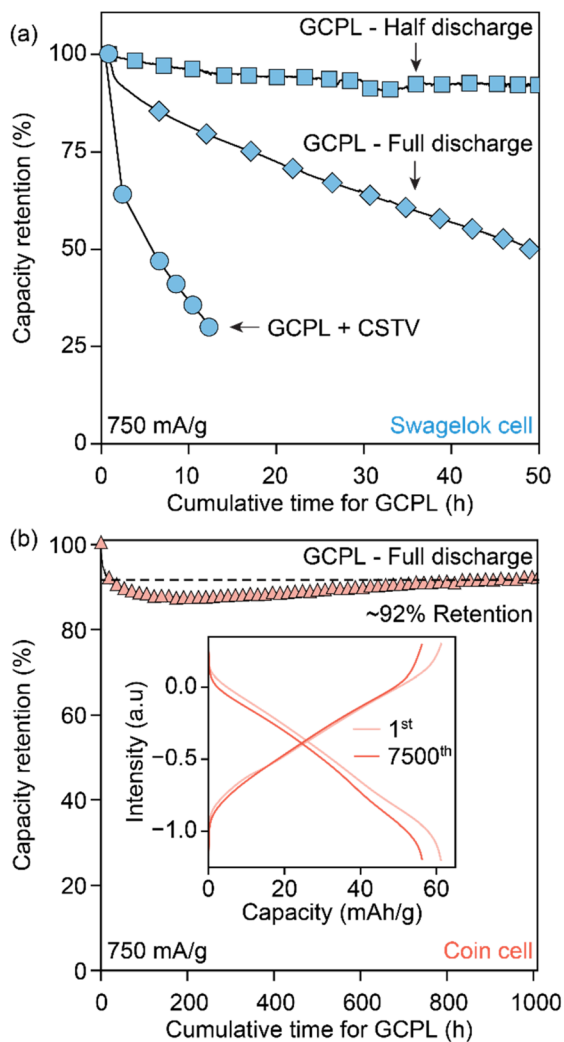
Fig. 6 (a) Cycling of Cu₃HHTP₂ in NaClO₄/ACN under different electrochemical conditions in Swagelok-type cells. GCPL cycling to half and full discharge states correspond to a current density of 750 mA g⁻¹ between 0.50 to −0.10 V and 0.50 to −0.75 V vs. Ag/AgCl, respectively. GCPL + CSTV corresponds to subjecting Cu₃HHTP₂ to a constant potential of −0.70 V vs. Ag/AgCl, with intermittent GCPL cycling at 750 mA g⁻¹ in the full potential window. (b) GCPL cycling of Cu₃HHTP₂ in a full potential window using NaClO₄/ACN electrolyte and a coin cell setup. Swagelok and coin cell setups use different electrolyte volumes of 2 mL and 50 μL, respectively.

mL⁻¹ or 0.52 nM in ACN, which should, in theory, rapidly saturate the electrolyte with HHTT, preventing continuous dissolution of Cu₃HHTT₂. Notably, all electrochemical data discussed so far were obtained in Swagelok-type cells that accommodate significant electrolyte volume (∼2 mL) that likely facilitates continuous dissolution of MOF during cycling (a picture of a Swagelok cell is shown in Fig. S23a†). We hypothesized that lowering the amount of electrolyte per active material mass could lead to a saturation of HHTT in the electrolyte, enabling longer cycling life. Indeed, tests performed in Swagelok cells using increasing electrolyte volumes of 1–15 mL mg⁻¹ of active material have delivered greater capacity retention in cells with lower electrolyte volumes (Fig. S24†). Furthermore,

tests performed in coin cells (a picture of a coin cell is shown in Fig. S23b†), which enabled the use of significantly less amount of electrolyte (50 μL or 0.05 mL mg⁻¹), delivered remarkable stability over 7500 cycles (or 1000 hours of continuous operation) compared to the tests in the Swagelok cells (Fig. 6b). The distinct performance of Cu₃HHTP₂ in different cell designs that accommodate different electrolyte volumes, while also differing in other aspects such as the pressure between electrodes and the area of the electrode surface, perhaps explain the different cycling performances noted for Cu₃HHTP₂ (ref. 33) and Cu₃THQ₂ (ref. 31 and 34) in this work and the previous reports. Overall, these studies further reaffirm that dissolution represents the primary mode of degradation for 2D cMOFs and the low solubilities of ligands in electrolytes could be leveraged for enhanced cycling stability.

Discussion

The discovery of electrode dissolution as the primary mode of electrochemical degradation for 2D cMOFs raises questions on what causes dissolution and how it proceeds. Although the combination of UV-vis, EQCM, and ICP-MS techniques has provided a qualitative and quantitative estimation of MOF dissolution, the true identity of the dissolved species remains unclear. An understanding of the dissolved species is essential in describing possible mechanisms for MOF dissolution. Nevertheless, the success of strategies aimed at saturating dissolution by using less electrolyte identifies low ligand solubility as a key design principle for future MOF design. Additionally, the series of stepwise electrochemical polarizations of cMOFs have identified a range of potentials (region 2) that exert the most detrimental influence on their cycling stability. Although *ex situ* characterizations have identified redox reactions to occur on both the ligand and metal nodes in this range of potentials, further investigations involving *in situ* and operando studies are necessary to capture the chemical and structural changes at the MX₄ linkages at these potentials. However, the dynamic and reversible nature of MX₄ linkages,[41–43] and the possibility of transient metal mediation in ligand-centered reduction processes,[11] together complicate the determination of their true influence on the cycling stability of cMOFs. Furthermore, it may also be construed as inappropriate to treat metal and ligand reduction as isolated processes when the material itself is electronically delocalized through π-d overlaps.[6,43] Overall, these factors present a need for deeper investigations into the effects of external polarization on MOF stability.

Although it is reasonable to expect that the conclusions drawn here may extend to other systems, such attempts must consider the limitations of the choice of materials and the experimental conditions used here. Specifically, the three MOFs investigated here share [CuO₄] linkages, and are studied under reductive potentials in water and ACN-based solutions. MOFs with different MX₄ linkages and their behavior under oxidative or purely capacitive electrochemical conditions may differ from this work. Additionally, several parameters such as the particle size, morphology (scanning microscopy images of Cu₃HHTT₂ in

Fig. S25†), electrode composition, type of binder, cell setup, mass loading, and electrolyte volume can all affect the cycling stability of a MOF.[44,45] Notably, the dissolution of MOFs shares similarities with the well-studied dissolution of organic electrode materials (OEMs), presenting opportunities for shared solutions.[46–53] Nevertheless, while the dissolution of OEMs typically provides strong visual cues, only Cu_3THQ_2 among the three MOFs studied here showed color in the electrolytes (Fig. S26†).

Conclusions

The electrochemical stability of 2D cMOFs and the potential mechanisms for their degradation during repeated charge–discharge cycling were investigated in three Cu-based 2D cMOFs. Cu_3HHTT_2, with a sparingly soluble ligand in aqueous electrolytes, delivered excellent cycling stability over 100 000 cycles or 1500 hours of operation. On the other hand, Cu_3THQ_2 and Cu_3HHTP_2 exhibited rapid degradation within the first 12 hours of their cycling. A comprehensive qualitative and quantitative analysis revealed that electrode dissolution is the primary mode of degradation for all three Cu-MOFs. A combination of UV-vis, ICP-MS, and EQCM studies revealed that up to 80% of the capacity loss in a MOF can proceed *via* electrode dissolution. Several factors that govern dissolution are investigated and solutions for mitigating dissolution are presented. Overall, these findings offer important design principles for targeted development and application of 2D cMOFs in EES.

Data availability

Data is made available upon a reasonable request.

Author contributions

J.-H. D. and H. B. conceived the project. G. M. R. D. and H. B. developed the methodology. G. M. R. D., S. P. S., J. L. M.-G. performed all experimental syntheses and investigations. T. C. performed XPS data collection and analysis. G. M. R. D., S. P. S., and H. B. prepared all visualizations. H. B. acquired the funding and supervised the project. G. M. R. D. and H. B. prepared the original draft. All authors have contributed to editing the manuscript and approved the final version of the manuscript.

Conflicts of interest

There are no conflicts to declare.

Acknowledgements

References

1 L. S. Xie, G. Skorupskii and M. Dincă, *Chem. Rev.*, 2020, **120**, 8536–8580.

2 M. Yu, R. Dong and X. Feng, *J. Am. Chem. Soc.*, 2020, **142**, 12903–12915.

3 C. N. Hong, A. B. Crom, J. I. Feldblyum and M. R. Lukatskaya, *Chem*, 2023, **9**, 798–822.

4 J. Park, M. Lee, D. Feng, Z. Huang, A. C. Hinckley, A. Yakovenko, X. Zou, Y. Cui and Z. Bao, *J. Am. Chem. Soc.*, 2018, **140**, 10315–10323.

5 J.-H. Dou, L. Sun, Y. Ge, W. Li, C. H. Hendon, J. Li, S. Gul, J. Yano, E. A. Stach and M. Dincă, *J. Am. Chem. Soc.*, 2017, **139**, 13608–13611.

6 K. Sakaushi and H. Nishihara, *Acc. Chem. Res.*, 2021, **54**, 3003–3015.

7 H. Banda, J.-H. Dou, T. Chen, N. J. Libretto, M. Chaudhary, G. M. Bernard, J. T. Miller, V. K. Michaelis and M. Dincă, *J. Am. Chem. Soc.*, 2021, **143**, 2285–2292.

8 H. Banda, J.-H. Dou, T. Chen, Y. Zhang and M. Dincă, *Angew. Chem.*, 2021, **133**, 27325–27331.

9 Z. Wu, D. Adekoya, X. Huang, M. J. Kiefel, J. Xie, W. Xu, Q. Zhang, D. Zhu and S. Zhang, *ACS Nano*, 2020, **14**, 12016–12026.

10 J. Park, A. C. Hinckley, Z. Huang, D. Feng, A. A. Yakovenko, M. Lee, S. Chen, X. Zou and Z. Bao, *J. Am. Chem. Soc.*, 2018, **140**, 14533–14537.

11 D. Rambabu, A. E. Lakraychi, J. Wang, L. Sieuw, D. Gupta, P. Apostol, G. Chanteux, T. Goossens, K. Robeyns and A. Vlad, *J. Am. Chem. Soc.*, 2021, **143**, 11641–11650.

12 Z. Wang, G. Wang, H. Qi, M. Wang, M. Wang, S. Park, H. Wang, M. Yu, U. Kaiser, A. Fery, S. Zhou, R. Dong and X. Feng, *Chem. Sci.*, 2020, **11**, 7665–7671.

13 J. Liu, Y. Zhou, Z. Xie, Y. Li, Y. Liu, J. Sun, Y. Ma, O. Terasaki and L. Chen, *Angew. Chem., Int. Ed.*, 2020, **59**, 1081–1086.

14 J. Yin, N. Li, M. Liu, Z. Li, X. Wang, M. Cheng, M. Zhong, W. Li, Y. Xu and X.-H. Bu, *Adv. Funct. Mater.*, 2023, **33**, 2211950.

15 M. Yang, X. Zeng, M. Xie, Y. Wang, J.-M. Xiao, R.-H. Chen, Z.-J. Yi, Y.-F. Huang, D.-S. Bin and D. Li, *J. Am. Chem. Soc.*, 2024, **146**, 6753–6762.

16 P. Apostol, S. M. Gali, A. Su, D. Tie, Y. Zhang, S. Pal, X. Lin, V. R. Bakuru, D. Rambabu, D. Beljonne, M. Dincă and A. Vlad, *J. Am. Chem. Soc.*, 2023, **145**, 24669–24677.

17 Y. Lu, Z. Hu, P. Petkov, S. Fu, H. Qi, C. Huang, Y. Liu, X. Huang, M. Wang, P. Zhang, U. Kaiser, M. Bonn, H. I. Wang, P. Samorì, E. Coronado, R. Dong and X. Feng, *J. Am. Chem. Soc.*, 2024, **146**, 2574–2582.

18 M. G. Campbell, D. Sheberla, S. F. Liu, T. M. Swager and M. Dincă, *Angew. Chem., Int. Ed.*, 2015, **54**, 4349–4352.

19 M. Hmadeh, Z. Lu, Z. Liu, F. Gándara, H. Furukawa, S. Wan, V. Augustyn, R. Chang, L. Liao, F. Zhou, E. Perre, V. Ozolins,

K. Suenaga, X. Duan, B. Dunn, Y. Yamamto, O. Terasaki and O. M. Yaghi, *Chem. Mater.*, 2012, **24**, 3511–3513.

20 D. Sheberla, L. Sun, M. A. Blood-Forsythe, S. Er, C. R. Wade, C. K. Brozek, A. Aspuru-Guzik and M. Dincă, *J. Am. Chem. Soc.*, 2014, **136**, 8859–8862.

21 S. Bi, H. Banda, M. Chen, L. Niu, M. Chen, T. Wu, J. Wang, R. Wang, J. Feng, T. Chen, M. Dincă, A. A. Kornyshev and G. Feng, *Nat. Mater.*, 2020, **19**, 552–558.

22 L. Guo, J. Sun, W. Zhang, L. Hou, L. Liang, Y. Liu and C. Yuan, *ChemSusChem*, 2019, **12**, 5051–5058.

23 R. Dong, Z. Zhang, D. C. Tranca, S. Zhou, M. Wang, P. Adler, Z. Liao, F. Liu, Y. Sun, W. Shi, Z. Zhang, E. Zschech, S. C. B. Mannsfeld, C. Felser and X. Feng, *Nat. Commun.*, 2018, **9**, 2637.

24 P. Zhang, M. Wang, Y. Liu, S. Yang, F. Wang, Y. Li, G. Chen, Z. Li, G. Wang, M. Zhu, R. Dong, M. Yu, O. G. Schmidt and X. Feng, *J. Am. Chem. Soc.*, 2021, **143**, 10168–10176.

25 P. Zhang, M. Wang, Y. Liu, Y. Fu, M. Gao, G. Wang, F. Wang, Z. Wang, G. Chen, S. Yang, Y. Liu, R. Dong, M. Yu, X. Lu and X. Feng, *J. Am. Chem. Soc.*, 2023, **145**, 6247–6256.

26 J. Zhang, G. Zhou, H.-I. Un, F. Zheng, K. Jastrzembski, M. Wang, Q. Guo, D. Mücke, H. Qi, Y. Lu, Z. Wang, Y. Liang, M. Löffler, U. Kaiser, T. Frauenheim, A. Mateo-Alonso, Z. Huang, H. Sirringhaus, X. Feng and R. Dong, *J. Am. Chem. Soc.*, 2023, **145**, 23630–23638.

27 D. Feng, T. Lei, M. R. Lukatskaya, J. Park, Z. Huang, M. Lee, L. Shaw, S. Chen, A. A. Yakovenko, A. Kulkarni, J. Xiao, K. Fredrickson, J. B. Tok, X. Zou, Y. Cui and Z. Bao, *Nat. Energy*, 2018, **3**, 30–36.

28 D. Sheberla, J. C. Bachman, J. S. Elias, C.-J. Sun, Y. Shao-Horn and M. Dincă, *Nat. Mater.*, 2017, **16**, 220–224.

29 M. R. Lukatskaya, D. Feng, S.-M. Bak, J. W. F. To, X.-Q. Yang, Y. Cui, J. I. Feldblyum and Z. Bao, *ACS Nano*, 2020, **14**, 15919–15925.

30 J. Yan, Y. Cui, M. Xie, G.-Z. Yang, D.-S. Bin and D. Li, *Angew. Chem., Int. Ed.*, 2021, **60**, 24467–24472.

31 Q. Chen, O. Adeniran, Z.-F. Liu, Z. Zhang and K. Awaga, *J. Am. Chem. Soc.*, 2023, **145**, 1062–1071.

32 K. W. Nam, S. S. Park, R. dos Reis, V. P. Dravid, H. Kim, C. A. Mirkin and J. F. Stoddart, *Nat. Commun.*, 2019, **10**, 4948.

33 J. M. Wrogemann, M. J. Lüther, P. Bärmann, M. Lounasvuori, A. Javed, M. Tiemann, R. Golnak, J. Xiao, T. Petit, T. Placke and M. Winter, *Angew. Chem., Int. Ed.*, 2023, **62**, e202303111.

34 Q. Jiang, P. Xiong, J. Liu, Z. Xie, Q. Wang, X.-Q. Yang, E. Hu, Y. Cao, J. Sun, Y. Xu and L. Chen, *Angew. Chem., Int. Ed.*, 2020, **59**, 5273–5277.

35 Y. Chen, Q. Zhu, K. Fan, Y. Gu, M. Sun, Z. Li, C. Zhang, Y. Wu, Q. Wang, S. Xu, J. Ma, C. Wang and W. Hu, *Angew. Chem., Int. Ed.*, 2021, **60**, 18769–18776.

36 J. W. Gittins, C. J. Balhatchet, Y. Chen, C. Liu, D. G. Madden, S. Britto, M. J. Golomb, A. Walsh, D. Fairen-Jimenez, S. E. Dutton and A. C. Forse, *J. Mater. Chem. A*, 2021, **9**, 16006–16015.

37 Y. Chen, Y. Zhang, Q. Huang, X. Lin, A. Zeb, Y. Wu, Z. Xu and X. Xu, *ACS Appl. Energy Mater.*, 2022, **5**, 7842–7873.

38 J.-H. Dou, M. Q. Arguilla, Y. Luo, J. Li, W. Zhang, L. Sun, J. L. Mancuso, L. Yang, T. Chen, L. R. Parent, G. Skorupskii, N. J. Libretto, C. Sun, M. C. Yang, P. V. Dip, E. J. Brignole, J. T. Miller, J. Kong, C. H. Hendon, J. Sun and M. Dincă, *Nat. Mater.*, 2021, **20**, 222–228.

39 J. Liu, D. Yang, Y. Zhou, G. Zhang, G. Xing, Y. Liu, Y. Ma, O. Terasaki, S. Yang and L. Chen, *Angew. Chem., Int. Ed.*, 2021, **60**, 14473–14479.

40 V. Augustyn, J. Come, M. A. Lowe, J. W. Kim, P.-L. Taberna, S. H. Tolbert, H. D. Abruña, P. Simon and B. Dunn, *Nat. Mater.*, 2013, **12**, 518–522.

41 J. Liu, D. Xie, X. Xu, L. Jiang, R. Si, W. Shi and P. Cheng, *Nat. Commun.*, 2021, **12**, 3131.

42 J. L. Obeso, M. T. Huxley, C. Leyva, J. Gabriel Flores, N. Martín-Guaregua, M. Viniegra, J. Aguilar-Pliego, J. Antonio de los Reyes, I. A. Ibarra and R. A. Peralta, *Coord. Chem. Rev.*, 2023, **496**, 215403.

43 K. Wada, K. Sakaushi, S. Sasaki and H. Nishihara, *Angew. Chem., Int. Ed.*, 2018, **57**, 8886–8890.

44 J. W. Gittins, C. J. Balhatchet, S. M. Fairclough and A. C. Forse, *Chem. Sci.*, 2022, **13**, 9210–9219.

45 S. P. Suman, G. M. R. Dontireddy, T. Chen, J. Wang, J.-H. Dou and H. Banda, *ACS Energy Lett.*, 2024, 1572–1580.

46 H. Banda, D. Damien, K. Nagarajan, A. Raj, M. Hariharan and M. M. Shaijumon, *Adv. Energy Mater.*, 2017, **7**, 1701316.

47 B. Esser, F. Dolhem, M. Becuwe, P. Poizot, A. Vlad and D. Brandell, *J. Power Sources*, 2021, **482**, 228814.

48 Y. Lu and J. Chen, *Nat. Rev. Chem.*, 2020, **4**, 127–142.

49 J. Kim, Y. Kim, J. Yoo, G. Kwon, Y. Ko and K. Kang, *Nat. Rev. Mater.*, 2023, **8**, 54–70.

50 J. Wang, A. E. Lakraychi, X. Liu, L. Sieuw, C. Morari, P. Poizot and A. Vlad, *Nat. Mater.*, 2021, **20**, 665–673.

51 H. Banda, D. Damien, K. Nagarajan, M. Hariharan and M. M. Shaijumon, *J. Mater. Chem. A*, 2015, **3**, 10453–10458.

52 T. Chen, H. Banda, J. Wang, J. J. Oppenheim, A. Franceschi and M. Dincă, *ACS Cent. Sci.*, 2024, **10**, 569–578.

53 T. Chen, H. Banda, L. Yang, J. Li, Y. Zhang, R. Parenti and M. Dincă, *Joule*, 2023, **7**, 986–1002.